Thermoelectric transport coefficients in mono-layer MoS2 and WSe2: Role of substrate, interface phonons, plasmon, and dynamic screening

Krishnendu Ghosh and Uttam Singisetti

Articles you may be interested in

Fabrication and comparison of MoS2 and WSe2 field-effect transistor biosensors
J. Vac. Sci. Technol. B **33**, 06FG01 (2015); 10.1116/1.4930040

Phonon scattering limited performance of monolayer MoS2 and WSe2 n-MOSFET
AIP Advances **5**, 027101 (2015); 10.1063/1.4907697

Phonon thermal conductivity of monolayer MoS2 sheet and nanoribbons
Appl. Phys. Lett. **103**, 133113 (2013); 10.1063/1.4823509

Thermoelectric performance of MX2 (M=Mo,W; X=S,Se) monolayers
J. Appl. Phys. **113**, 104304 (2013); 10.1063/1.4794363

Thermoelectric performance of Ni y Mo 3 Sb 7 − x Te x (y ≤ 0.1 , 1.5 ≤ x ≤ 1.7)
J. Appl. Phys. **105**, 053703 (2009); 10.1063/1.3086641

Thermoelectric transport coefficients in mono-layer MoS₂ and WSe₂: Role of substrate, interface phonons, plasmon, and dynamic screening

Krishnendu Ghosh[a] and Uttam Singisetti[b]
Electrical Engineering Department, University at Buffalo, Buffalo, New York 14260, USA

The thermoelectric transport coefficients of electrons in two recently emerged transition metal di-chalcogenides (TMD), MoS₂ and WSe₂, are calculated by solving Boltzmann transport equation using Rode's iterative technique in the diffusive transport regime and the coupled current (electrical and heat) equations. Scattering from remote phonons along with the hybridization of TMD plasmon with remote phonon modes and dynamic screening under linear polarization response are investigated in TMDs sitting on a dielectric environment. The transport coefficients are obtained for a varying range of temperature and doping density for three different types of substrates—SiO₂, Al₂O₃, and HfO₂. The Seebeck co-efficient for MoS₂ and WSe₂ is found to be higher than 3D semiconductors even with diffusive transport. The electronic thermal conductivity is found to be low, however, the thermoelectric figure of merit is limited by the high phonon thermal conductivity. It is found that judicious selection of a dielectric environment based on temperature of operation and carrier density is crucial to optimize the thermoelectric performance of TMD materials. © 2015 AIP Publishing LLC. [http://dx.doi.org/10.1063/1.4932140]

I. INTRODUCTION

Transition metal di-chalcogenides (TMD) have recently attracted unprecedented attention[1–10] in the electron device community especially as a replacement of silicon for transistor channels. Unlike graphene, these materials have an intrinsic band-gap which makes them suitable for transistor channels reminiscent of an ideal switch for digital logic applications. Among the TMDs, MoS₂ has been investigated extensively, in particular, due to its abundance in nature.[1–6] WSe₂ has got attention[7–10] due to its intrinsic doping property which allows the scope for observance of ambipolar characteristic.[9] However, in addition to be studied as potential transistor channel semiconductors, these materials have interesting mechanical, optical, and thermoelectric properties that could be used for various emerging applications.[6] Thermoelectric properties of these materials, in particular, could have significant technological importance due to their capability of converting thermal energy to electrical energy efficiently and vice-versa.[11–15] Important thermoelectric properties of interest include Seebeck coefficient (α), Peltier coefficient (π), and thermal conductivity (κ_e). Low dimensional systems have been proposed for thermoelectric applications due to their intrinsic advantages.[16–18] Among 2D materials, nanostructured graphene,[19] graphene/BN superlattices[20] have been investigated recently for thermoelectric applications, and other 2D materials have been proposed as potential candidates for thermoelectric applications.[21] Though extensive research has been carried out on the electronic properties of TMDs, their thermoelectric properties have not been studied much. Recent *ab initio* calculations[22–25] have shown the thermoelectric properties of the

TMDs. These reports have considered either ballistic transport or a constant energy independent mean free path and scattering time. However, these assumptions are not consistent with the measured transport properties of the TMDs. Indeed, a strong evidence of diffusive transport is reflected in the low carrier mobility of these materials. Moreover, Rode[26] has shown that the Seebeck coefficient does not depend on the absolute value of the scattering rates, rather it depends on how the scattering rate depends on electron energy. Detailed quantitative calculations and careful analysis in this work have shown that it is important to consider the effect of scattering as they do impact the thermoelectric properties significantly. A paramount role is played by the substrate on which the TMD is grown or transferred. Like graphene,[27] TMDs also suffer from scattering mediated by remote optical phonon modes of the substrate. On one side, high-k substrates suppress the Coulomb scattering,[28,29] while on the contrary, their strong optical modes cause additional scattering.[29] Similar to mobility calculations, this trade-off becomes important for calculation of thermoelectric transport coefficients too.

In this paper, we solve the Boltzmann transport equation (BTE) and the coupled electrical and thermal current equations for MoS₂ and WSe₂ to extract thermoelectric transport coefficients. Scatterings from donor impurities, longitudinal optical (LO) polar modes, acoustic deformation potential, and substrate induced remote phonon modes are taken into account. We use Rode's iterative method in order to take into account the inelastic and anisotropic nature of the electron-LO mode scattering and also electron-remote phonon mode scattering.[30,31] A dynamic screening model is used assuming random phase approximation. The organization of the paper is as follows. In Section II, we start with the procedure used to solve the BTE and the coupled current equations. In Section III, we briefly discuss the models for

[a]Email: kghosh3@buffalo.edu. Tel.: 716-645-1017.
[b]Email: uttamsin@buffalo.edu. Tel.: 716-645-1536; Fax: 716-645-3656.

elastic scattering mechanisms and the Frölich electron-LO mode interaction. In Section IV, we discuss the formation of interface plasmon-phonon (IPP) modes due to coupling of plasmon with the remote phonon modes. Here, we also talk about calculation of corresponding scattering field strength and matrix elements. Section V covers the details of screening calculation, including discussion on Landau damping. In Section VI, we give insight on our results and findings of this study followed by conclusion in Section VII.

II. THE BTE AND THE COUPLED CURRENT EQUATIONS

The electrical current density due to flow of electrons is given by the contribution from the non-symmetric part of the electronic distribution function

$$J_x = -\frac{e}{\Omega} \sum_k v_x(\boldsymbol{k}) f_A(\boldsymbol{k}). \tag{1}$$

Here, v_x is the group velocity of electrons in the transport direction, $f_A(\boldsymbol{k})$ is the non-symmetric part of the electronic distribution which is discussed later, $\boldsymbol{k}$ is the electron wave-vector, and Ω is a normalization area. On the other hand, the heat current density due to electron flow is given by the kinetic energy flow contribution from the non-symmetric part of the electronic distribution function

$$J_{Qx} = \frac{1}{\Omega} \sum_k [E(\boldsymbol{k}) - E_F] v_x(\boldsymbol{k}) f_A(\boldsymbol{k}). \tag{2}$$

Here, E is the electron energy and E_F is the chemical potential. We calculate the non-symmetric part of the electronic distribution function using Rode's iterative calculation.[26] Under low electric fields, the entire distribution function can be written as

$$f(\boldsymbol{k}) = f_0(k) + g(k)\cos\theta. \tag{3}$$

Here, f_0 is the equilibrium Fermi-Dirac distribution and θ is the angle between the applied electric field direction and $\boldsymbol{k}$. The point to be noted here is that g only depends on the magnitude of the electron wave-vectors. Rode's iteration solves for g using the following conformal mapping:

$$g_{i+1} = \frac{S_{in}(g_i') - \frac{eF}{\hbar}\frac{\partial f_0(k)}{\partial k} - v\frac{\partial f_0}{\partial x}}{S_{out}(k) + 1/\tau_m(k)}. \tag{4}$$

Here, S_{out} and S_{in} are the net out-scattering rate and in-scattering rate, respectively. τ_m is the momentum relaxation time for the elastic scattering processes discussed in Section III. F is the applied parallel electric field, which should be low enough for Eq. (3) to be good. $\frac{\partial f_0}{\partial x}$ can be expressed in terms of $\frac{\partial T}{\partial x}$ (which is done in Ref. 26 for a bulk system and in Eq. (C8) of this work for a 2D system). For calculating S_{out} and S_{in} from the scattering matrix elements, we follow the procedure described in our previous work for a 2DEG system.[31] The iteration (Eq. (4)) begins with a g_0 given by the relaxation time approximation (RTA). Once the

distribution converges, J_x and J_{Qx} can readily be calculated from Eqs. (1) and (2), respectively.

Fig. 1 shows the outline of the entire calculation. First, we consider the device under isothermal condition. We calculate the drift mobility from scattering matrix elements and store it for later use. Next, we apply a small temperature gradient ($\frac{\partial T}{\partial x} = 10^3$ K/m) with the device ends being electrically shorted and compute the corresponding spatial gradient of the Fermi-Dirac distribution function. Using this and the previously calculated scattering matrix elements, we run Rode's iteration again. Please note here, since the two ends are shorted, the second term on the numerator of Eq. (4) vanishes ($F = 0$). Once the Rode's iteration converges, the electric current density (J_x) and the heat current density (J_{Qx}) can be calculated from which the transport coefficients can be extracted from their definition[32]

$$J_x = \sigma_x \frac{\partial E_F}{\partial x} - \frac{B_x}{T^2}\frac{\partial T}{\partial x}, \tag{5a}$$

$$J_{Qx} = p_x \frac{\partial E_F}{\partial x} - \frac{K_x}{T^2}\frac{\partial T}{\partial x}. \tag{5b}$$

Here, σ_x, B_x, p_x, and K_x are the transport coefficients. An important point to be noted here is that we assume an isotropic crystal in two dimensions so that the transport coefficient tensors are diagonal. The isothermal calculations previously stored the values of σ_x and p_x. The remaining two coefficients can be extracted from the J_x and J_{Qx} calculated with the temperature gradient.

The thermoelectric properties of interest that can be computed from here are the Seebeck coefficient, Peltier coefficient, and thermal conductivity (electronic contribution). They are related to the transport coefficients by the following relations:[32]
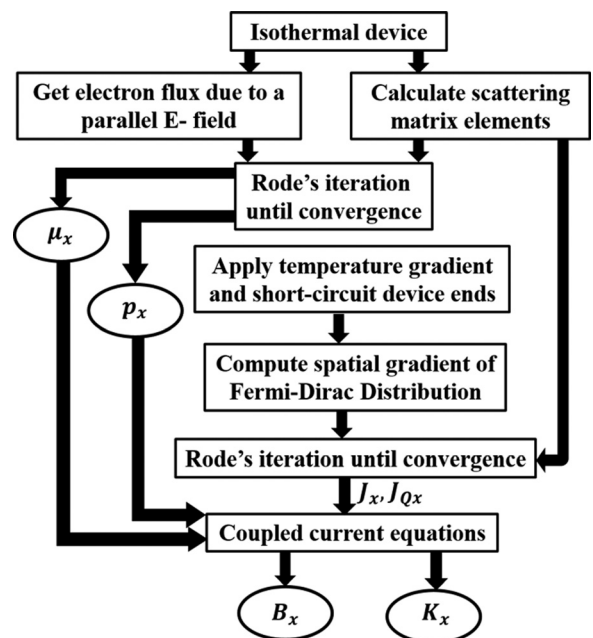

FIG. 1. Outline of the procedure to calculate the mobility and thermoelectric coefficients by solving solve coupled BTE using Rode's method.

$$\alpha = \frac{B_x}{\sigma_x T^2}, \quad \pi = \frac{p_x}{\sigma_x}, \quad \kappa_e = \frac{K_x - \frac{p_x B_x}{\sigma_x}}{T^2},$$

α, π, and κ_e are the Seebeck coefficient, Peltier coefficient, and thermal conductivity, respectively.

III. INTRINSIC SCATTERING MECHANISMS

Several intrinsic scattering mechanisms as discussed in the introduction make the transport diffusive in TMDs. We consider impurity and acoustic deformation potential scattering matrix elements as were considered in references 29 and hence we do not describe them here. For the impurity scattering, we consider ionized donor scattering ($N_D = n_S$, where n_S is the electron concentration and N_D is the ionized donor impurity concentration) without any additional impurities. The momentum relaxation times from each of these two types of scattering mechanism are calculated and are plugged in the Rode's iteration loop (Eq. (4)) as the elastic scattering parameter. Another very important scattering mechanism originates from the electron–LO phonon interaction. However, the conventional macroscopic models do not hold good for atomistically thin semiconductors as pointed out by Kaasbjerg *et al.*[33] We first follow their analytic approach (Eq. (9) of Ref. 33) to find the polar LO phonon scattering rate. Next, we employ dynamic screening on the electron-LO phonon coupling matrix to improve the accuracy of the calculation; the dynamic screening behavior is discussed in Section V.

IV. SCATTERING BY REMOTE INTERFACE PHONONS

The presence of remote phonon modes at the interface of a dielectric and a semiconductor has been studied extensively for 3D and 2D semiconductors.[34–38] But, according to the best of our knowledge, coupling of such remote phonon modes with the plasmon was not discussed for TMDs, though it is discussed in details for graphene and 2DEGs.[27,39] We consider a simple geometry, relevant for thermoelectric applications, shown in the inset of Fig. 2(a) where a TMD material is sitting on a substrate and the other side of the interface is air.

A. Coupled plasmon-remote phonon modes

In such a system, the potential due to the remote phonon modes can be written as

$$\varphi_q^\nu(z) = A_{q,\omega_q^\nu} \exp(-qz); \quad z > 0$$
$$= B_{q,\omega_q^\nu} \exp(qz); \quad z < 0, \tag{6}$$

q, ω_q^ν represent the wave-vector and energy of the phonon field with ν being the mode index. Implementing Dirichlet and Neumann boundaries, we obtain the secular equation

$$\varepsilon_{TMD}(q, \omega_q^\nu) + \varepsilon_{sub}(q, \omega_q^\nu) = 0. \tag{7}$$

Here, $\varepsilon_{TMD}(q, \omega_q^\nu)$ and $\varepsilon_{sub}(q, \omega_q^\nu)$ are the two out-of plane dynamic dielectric constants of the TMD and the substrate, respectively. In long-wavelength limit, they have the following form:

$$\varepsilon_{TMD}(q, \omega_q^\nu) = \varepsilon_{TMD}^\infty \left(1 - \frac{\omega_P^2}{\omega^2}\right), \tag{8a}$$

$$\varepsilon_{sub}(q, \omega_q^\nu) = \varepsilon_{sub}^\infty + \frac{\varepsilon_{sub}^0 - \varepsilon_{sub}^{int}}{\omega_{TO,1}^2 - (\omega_q^\nu)^2} \omega_{TO,1}^2$$
$$+ \frac{\varepsilon_{sub}^{int} - \varepsilon_{sub}^\infty}{\omega_{TO,2}^2 - (\omega_q^\nu)^2} \omega_{TO,2}^2, \tag{8b}$$

ε_i^∞ and ε_i^0 are the high frequency and static dielectric constants of the corresponding materials. ε_{sub}^{int} is an intermediate dielectric constant defined to distinguish the contributions of the two TO phonon modes to the net dielectric constant of
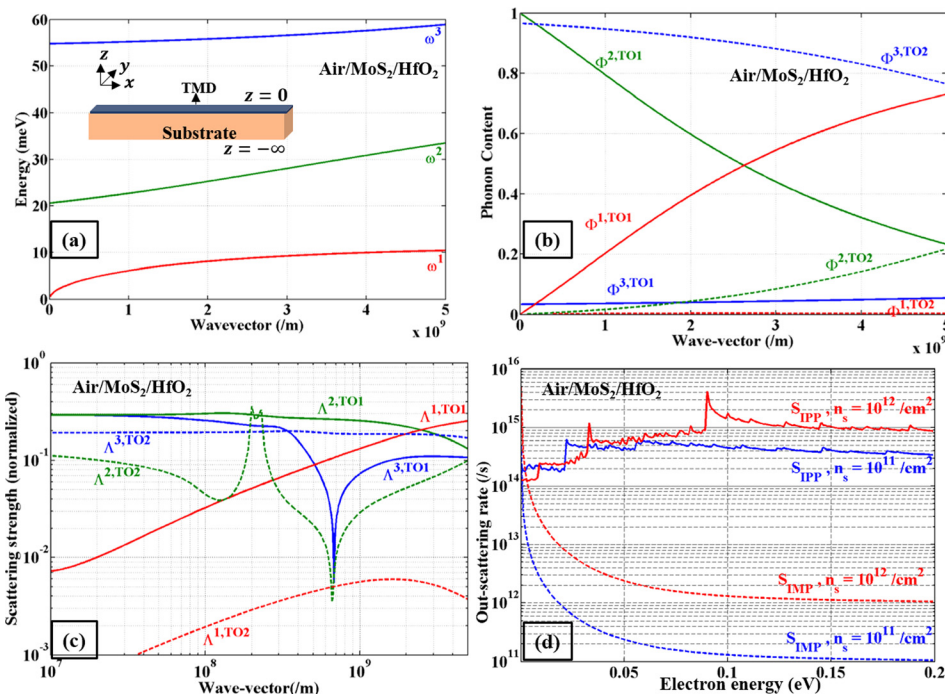

FIG. 2. (a) Dispersion of the coupled IPP modes for MoS$_2$ on HfO$_2$ dielectric (inset) device geometry and axes. (b) Phonon content in each IPP mode. The solid lines show content of first TO mode, while the dashed ones show content of second TO mode. (c) Normalized scattering strength of the IPP modes due to the phonon content. The solid lines show scattering strength contribution of first TO mode, while the dashed ones show the same for second TO mode. (d) The out-scattering rates (S_{out}) for electron-IPP interaction for two different electron densities for MoS$_2$ on HfO$_2$ are shown in solid lines. The corresponding impurity scattering rates are also shown for comparison (dashed lines).

TABLE I. TO-phonon and dielectric constants of different substrates (from Ref. 37).

Properties	Substrate		
	SiO$_2$	Al$_2$O$_3$	HfO$_2$
$\omega_{TO,1}$ (meV)	55.6	48.18	12.40
$\omega_{TO,2}$ (meV)	138.1	71.41	48.35
ε_{sub}^0	3.9	12.53	22
ε_{sub}^{int}	2.8	6.58	7.27
ε_{sub}^∞	2.5	3.2	5.03

TABLE II. Properties of different TMDs.

Properties	TMD	
	MoS$_2$	WSe$_2$
ω_{LO} (meV)	48[a]	32[b]
m_e	0.48[a]	0.33[c]
ε_{TMD}^∞ [d]	4	4

[a]Reference 33.
[b]Reference 47.
[c]Reference 48.
[d]The high frequency dielectric constants of TMDs are taken to be equal to their static values due to negligible LO-TO splitting. Also, these values for the two TMDs are taken to be equal. They are indeed very close to each other.[49]

the substrate. ω_P is the plasmon energy of the TMD for which we take the form of 2D plasmon dispersion discussed in Ref. 40. ε_{TMD}^∞ is the high frequency dielectric constant of the TMD. Detailed discussion on the TMD dielectric constant and plasmon vibration is done later in Section V. $\omega_{TO,1}$ and $\omega_{TO,2}$ are the TO mode energies in the substrates. The list of substrate parameters is given in Table I, while Table II lists the materials parameters used for MoS$_2$ and WSe$_2$. Solving the secular equation (Eq. (7)), we obtain the dispersion relation for the IPP modes for MoS$_2$ on HfO$_2$ as shown in the main panel of Fig. 2(a). It can be seen that there is significant coupling between the surface modes and the plasmon mode for the bottom two modes which will impact the electron scattering rate.

B. Phonon content and scattering strength

Since only the phonon part of the IPP coupled modes effectively causes exchange of energy between surface modes and electrons,[41] we need to separate out the phonon contributions from these coupled modes. The phonon content is extracted following the method described in Refs. 27, 31, 39, and 41. The phonon content of the three modes in Fig. 2(a) is plotted in Fig. 2(b) ($\Phi^{\nu,TOi}$, TOi is the ith TO mode of the substrate).

Having obtained the dispersion relation and the phonon content of the coupled IPP modes, we calculate[37] the coefficient A_{q,ω_q^ν} in Eq. (6) ($= B_{q,\omega_q^\nu}$, from Dirichlet boundary condition at $z = 0$) by equating the electrostatic energy of the scattering field with the ground state quantum mechanical energy of the modes

$$\int \varphi_q^\nu(z)\rho_q^\nu(z)dz = \frac{1}{2}\hbar\omega_q^\nu. \tag{9}$$

Here, ρ_q^ν is the polarization charge induced by the scattering field associated with the phonon at (q, ω_q^ν). The polarization charge can be obtained by solving the Poisson's equation with a tailored dielectric function.[37] By tailored dielectric function, we mean that we want to separate out the contribution of each phonon mode in inducing that polarization charge. This can be done by separating out each phonon contribution in the dielectric function of the substrate. The details of this calculation are given in Appendix A. Here, we give the final form of the phonon contributed screened scattering field strength for each mode

$$\Lambda^{\nu,TOi}(q) = \sqrt{\frac{\hbar\omega_q^\nu}{\varepsilon_0 q}\left(\frac{1}{\varepsilon_{sub}^{\nu,-TOi}(q,\omega_q^\nu) + 1 + \frac{e^2\Pi(q,\omega)}{2q}\phi_1} - \frac{1}{\varepsilon_{sub}^{\nu,+TOi}(q,\omega_q^\nu) + 1 + \frac{e^2\Pi(q,\omega)}{2q}\phi_1}\right)\Phi^{\nu,TOi}}, \tag{10}$$

which looks analogous to what was derived for top gated graphene device in Ref. 39. Here, $\varepsilon_{sub}^{\nu,-TOi}$ and $\varepsilon_{sub}^{\nu,+TOi}$ are the mentioned tailored dielectric functions discussed in Appendix A. The term $\frac{e^2\Pi(q,\omega)}{2q}\phi_1$ comes from electronic polarization inside the TMD which is discussed in Section V. The scattering strengths calculated this way are plotted (normalized by $\sqrt{\frac{\hbar\omega_q^\nu}{\varepsilon_0 q}}$) in Fig. 2(c).

C. Electron-IPP coupling matrix and scattering rate

Once the scattering field strength is obtained, calculation of the coupling matrix elements with the electrons is straightforward. The interaction Hamiltonian can be written as

$$H_q^\nu = \sqrt{\sum_{i=1,2}(\Lambda^{\nu,TOi}(q))^2}(e^{iq.r}a_q^{\nu+} + e^{-iq.r}a_q^\nu). \tag{11}$$

Here, $a_q^{\nu+}$ and a_q^ν are the IPP creation and annihilation operators. To calculate the electron-IPP coupling matrix, for simplicity, we take the out-of-plane electronic wave function to be sinusoidal and compute the matrix elements as

$$M_q^\nu = \frac{2}{t}\int_0^t H_q^\nu \exp(-qz)\sin^2\left(\frac{\pi z}{t}\right)dz, \tag{12}$$

t is the thickness of the TMD, taken to be 5 Å in this work. The retardation effects[34] at very small wave-vectors
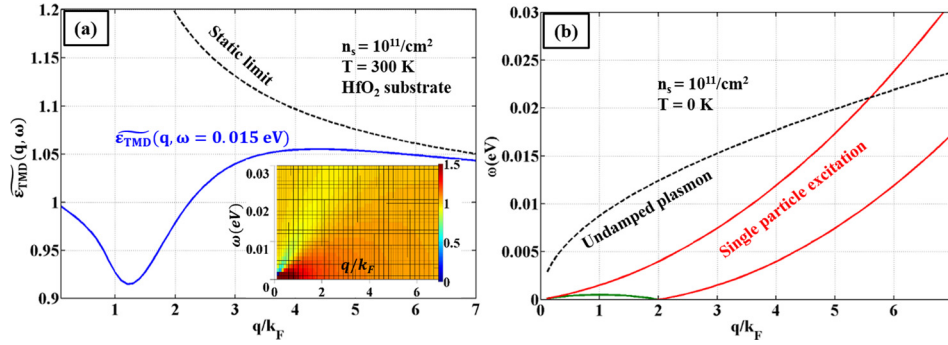
FIG. 3. (a) Comparison of dynamic dielectric constant (normalized with respect to $\varepsilon_{TMD}^{\infty}$, $\widetilde{\varepsilon_{TMD}}(q,\omega) = \varepsilon_{TMD}(q,\omega)/\varepsilon_{TMD}^{\infty}$) with the static Thomas-Fermi limit (inset) shows the contour plot of $\widetilde{\varepsilon_{TMD}}(q,\omega)$ in the (q,ω) plane. (b) The single particle-excitation (SPE) boundaries—the red ones show boundaries for SP emission, while the green one shows that for absorption. In the SPE region, plasmon contribution to screening is reduced due to Landau damping. The undamped plasmon response is shown in black dashed line.

$(q \approx \frac{\omega_{TO}}{c}$, c is the speed of light in that medium) are safely ignored. After the matrix elements are calculated, they can be plugged into the Fermi Golden rule to get the scattering probabilities ($P(\mathbf{k}, \mathbf{k}')$) from an electronic state $\mathbf{k}$ to $\mathbf{k}'$. These scattering probabilities are used in the out-scattering equation of our previous work (Eq. (19b) of Ref. 31). The calculated out-scattering rate S_{IPP} is plotted in Fig. 2(d) for two different electron densities (n_s) and also for comparison, the calculated impurity mediated momentum relaxation rate (S_{IMP}) is plotted. The sharp kinks in S_{IPP} arise due to onset of phonon emission, while the tiny jitters come due to numerical gridding of the q space. The essential point to note here, which will be crucial while analyzing thermoelectric properties, is that at low energy ranges, the impurity scattering rate swiftly drops well below the phonon scattering rate. Also, as we increase the electron densities, the impurity scattering rate increases due to more number of donor impurities (Note: $N_D = n_s$ here). The dependence of phonon scattering rate on n_s is an interplay between enhanced screening, which tries to cut down the rate and an expanding Fermi radius, which tries to increase the rate. For this particular case of HfO$_2$, shown in Fig. 2(d), enhancement of screening with carrier density is not pronounced due to a large dielectric mismatch between the substrate and the TMD. Hence, the scattering rate increases slightly with n$_s$.

V. DYNAMIC SCREENING

We include dynamic scattering with finite temperature polarizability in the scattering rate calculations following the random phase approximation.[40,42] The dynamic dielectric function can be obtained from polarization as

$$\varepsilon_{TMD}(q,\omega) = \varepsilon_{TMD}^{\infty}\left(1 + \frac{e^2 \Pi(q,\omega)}{2\varepsilon_{TMD}^{\infty}q}(\phi_1 + \phi_2)\right), \quad (13)$$

where ($\Pi(q,\omega)$) is the dynamic polarizability. ϕ_1 and ϕ_2 are form factor and dielectric mismatch factor, respectively, defined in Ref. 43. The dielectric function calculated in this way is shown in the contour plot shown in the inset in Fig. 3(a). The main panel of Fig. 3(a) shows the comparison between a Thomas-Fermi like static screening and a dynamic screening which clearly shows the necessity of taking

dynamic screening at long wave-length limit which is explained further in the next paragraph. In the long-wavelength limit, the TMD dielectric function given in Eq. (13) can be expressed as the one given in Eq. (8a).

Plasmons can absorb (emit) energy from (to) an external electro-magnetic field which leads to damped oscillation, known as Landau damping. Fig. 3(b) shows the region of plasmon damping due to the interaction of it with an external field (known as single particle excitation (SPE)). The emission and absorption boundaries of SPE regions are calculated from momentum and energy conservation in a 2D system. If we observe the plot in Fig. 3(a), we see that the plasmon has a significant role in the dynamic screening process. In the long-wavelength limit, when the plasmon energy lies below the phonon energy (shown as $\omega = 0.015$ eV in Fig. 3(a)), with increasing wave-vector effective dielectric constant drops due to *anti-screening* effect by the plasmon, however as the plasmon energy approaches the phonon energy, the anti-screening effect decreases and screening tends to begin. Finally, the onset of SPE cuts down the effect of the plasmon and at large wave-vectors, the normalized dielectric constant approaches unity. On the other hand, the static screening limit assumes a fully responsive plasmon outside SPE region and thus the anti-screening effect is not captured.

VI. RESULTS AND DISCUSSIONS

Having set-up the theoretical details of our calculation, the transport coefficients and the corresponding thermoelectric figure-of-merits are calculated for a temperature range of 50 K–500 K, keeping the density of electrons within the TMD fixed at 10^{11}/cm^2 and similarly, the same are calculated for an electron density range of 10^{11}–10^{13}/cm^2 with the temperature fixed at 300 K. All these calculations are done for two different TMDs: MoS$_2$ and WSe$_2$, each with three different substrates (SiO$_2$, Al$_2$O$_3$, and HfO$_2$). While mobility is extracted from isothermal device, transport coefficients are calculated for a temperature gradient of 10^3 K/m. The transport coefficients do not depend on the temperature gradient, however the results are good only in the limit of a small temperature gradient since a large value of it will make the scattering rates vary across the length of the device. The computational details and convergence rate of the
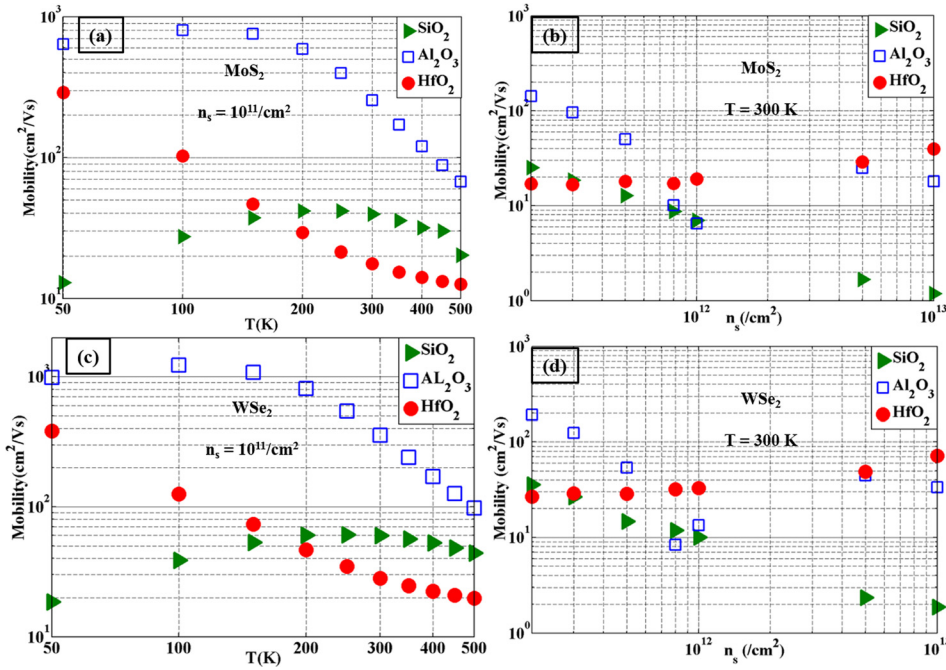
FIG. 4. (a) and (b) Dependence of mobility for MoS_2 on temperature and electron density for different dielectric substrates; (c) and (d) similar plots for WSe_2. The plots with respect to n_s ((b) and (d)) begin from $n_s = 2 \times 10^{11}/cm^2$.

calculation are given in Appendix B. We discuss the results below.

A. Mobility

The calculated mobility values are plotted in Figs. 4(a)–4(d). Figs. 4(a) and 4(c) show the effect of temperature for MoS_2 and WSe_2, respectively, while Figs. 4(b) and 4(d) show the corresponding effects of electron density at 300 K. It can be seen from Figs. 4(a) and 4(c) that as the temperature is increased, the mobility on SiO_2 supported TMD increases initially which is a signature of the donor impurity scattering limited mobility. Then the mobility starts dropping from around 200 K which signifies two important things. First is the onset of the remote phonon scattering mediated by the TO mode of SiO_2 that occurs around 55 meV and the second crucial point is the degradation of the polarizability of the TMD electrons due to thermal randomization. Now if we take a look at the mobility values for TMD supported by Al_2O_3, we find that the mobility at low temperature is more than an order higher than that supported by SiO_2 which is a characteristic of better dielectric environment screening the impurity scattering. The mobility starts dropping around 150 K due to the onset of remote phonon scattering by the lower TO mode of Al_2O_3 (48 meV). At higher temperature, we see that mobility drops more rapidly compared to that in case of SiO_2 which is because of the nearby second TO mode of Al_2O_3 at 71 meV, while SiO_2 has the second TO mode at a very high energy at 138 meV. The degradation of polarizability with temperature affects the overall screening less in case of Al_2O_3 than that in SiO_2 because of a higher dielectric mismatch (difference between dielectric constant of substrate and TMD) in case of Al_2O_3. Finally, we focus on HfO_2 supported TMD. Here, we do not see any sign of donor impurity scattering for strong dielectric environment screening and also for the very early onset of remote phonon scattering by the lower TO mode of HfO_2 at 12 meV.

Next, we discuss the electron density dependence. From Figs. 4(b) and 4(d), we see that with increasing n_s, SiO_2 supported TMD shows decline in mobility due to enhanced impurity scattering (note $N_D = n_s$), while HfO_2 shows slight improvement in mobility due to enhanced screening by electrons. Al_2O_3 shows non-monotonic trend due to a strong interplay between remote-phonon scattering and impurity scattering.

B. Thermoelectric coefficients

The calculated Seebeck coefficients for MoS_2 and WSe_2 under different temperature and different electron density are plotted in Figs. 5(a)–5(d). The Seebeck coefficient in a non-degenerate 2D material can be expressed under RTA (see Appendix C) as $-\frac{k_B}{e}\left(2 - r - \frac{E_F}{k_B T}\right)$, where r is the energy exponent in the scattering rate. At low temperatures, the Seebeck coefficients obtained from the analytical expression (Eq. (C12), assuming RTA) agree well with the detailed calculation using Rode's method (see Fig. 10) due to the reduced phonon scatterings (both LO and IPP) at low temperatures. It deviates at higher temperatures when the phonon scattering rate increases. However, an important message, similar to that discussed before for bulk materials,[26] to note from the given expression is that the Seebeck coefficient is given by the scattering rate dependence on energy (r in Eq. (C12)) and not on the absolute values of the scattering rates. As can be seen from Fig. 2(d), impurity scattering at lower energies drops swiftly with energy. A simple fitting gives a $E^{-1.1}$ roll off, while at a similar energy range, IPP (and also LO) phonon scattering rate depends weakly on energy. The comparison between the analytical calculation and the computed data for SiO_2 is shown in Fig. 10. At higher temperature, r deviates from -1.1 because of the onset of phonon emission process and temperature dependent polarizability and more importantly, RTA becomes invalid. To discuss the effect of substrates at low temperature, we
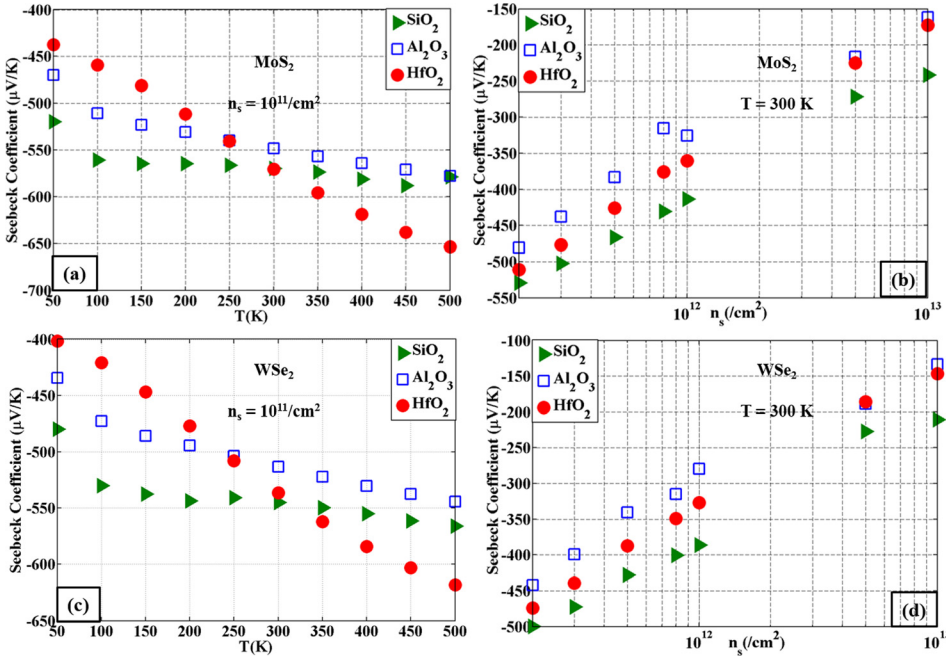
FIG. 5. (a) and (b) Dependence of Seebeck coefficient for MoS$_2$ on temperature and electron density; (c) and (d) similar plots for WSe$_2$. The plots with respect to n$_s$ ((b) and (d)) begin from n$_s$ = 2 × 10^{11}/cm^2.

note that most of the electrons stay near the edge of the conduction band where the dominant scattering mechanism is the one mediated by impurities. Hence, as can be seen from Figs. 5(a) and 5(c), at low temperature, SiO$_2$ can produce a better Seebeck coefficient, while HfO$_2$ being a source of dominant IPP scattering (even at low temperature from the lower TO mode of HfO$_2$) produces low Seebeck coefficient. The cross-over near room temperature clearly reflects the temperature dependent influence of the two opposite substrates (in terms of their dielectric constant) in bringing out an optimum thermoelectric power from a TMD.

Figs. 5(b) and 5(d) show the dependence of Seebeck coefficient on density. Increasing density reduces the Seebeck coefficient (since a higher Fermi Level reduces the

effect of temperature gradient on the spatial variation of Fermi Level) which is well known.[26] Our goal in this paper is to study the effect of the substrates. To get an intuitive insight, we can crudely rewrite the analytical expression for Seebeck coefficient as $-\frac{k_B}{e}\left(2 - r - \ln\left(\frac{\pi\hbar^2 n_S}{2m^* k_B T}\right)\right)$. At low value of n_S, the logarithmic term dominates (with a negative value) and all substrates produce similar Seebeck coefficient. However as we increase n_S and approach 10^{13}, the logarithmic term tends to vanish and the Seebeck coefficient is determined by r which depends on the substrate we choose. Hence, SiO$_2$ shows a higher Seebeck coefficient due to impurity dominated scattering. The corresponding Peltier coefficient for each case is plotted in Figs. 6(a)–6(d). The effect
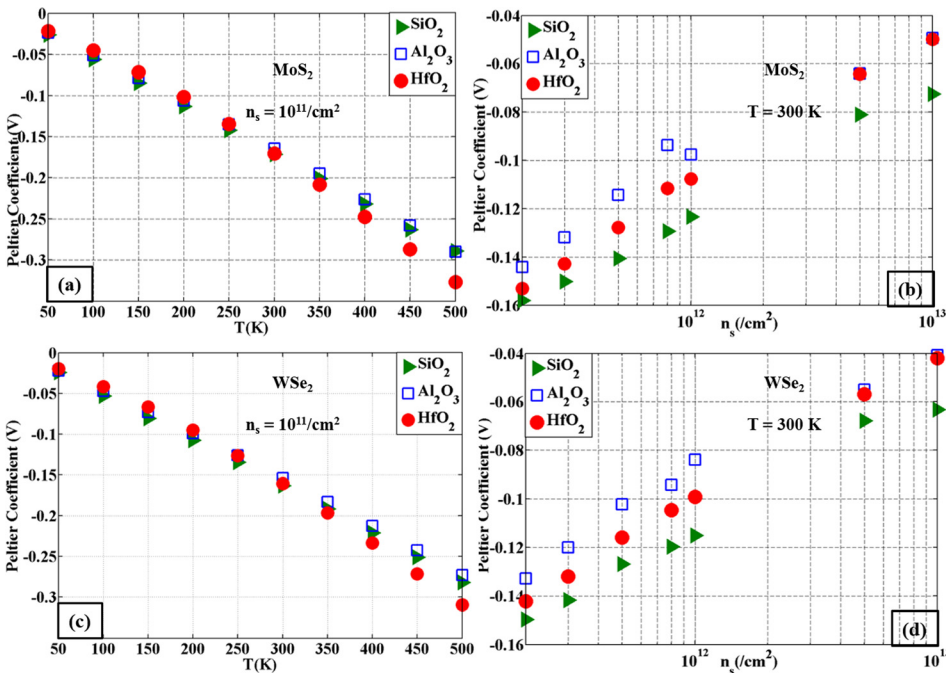

FIG. 6. (a) and (b) Dependence of Peltier coefficient for MoS$_2$ on temperature and electron density; (c) and (d) similar plots for WSe$_2$. The plots with respect to n$_s$ ((b) and (d)) begin from n$_s$ = 2 × 10^{11}/cm^2.
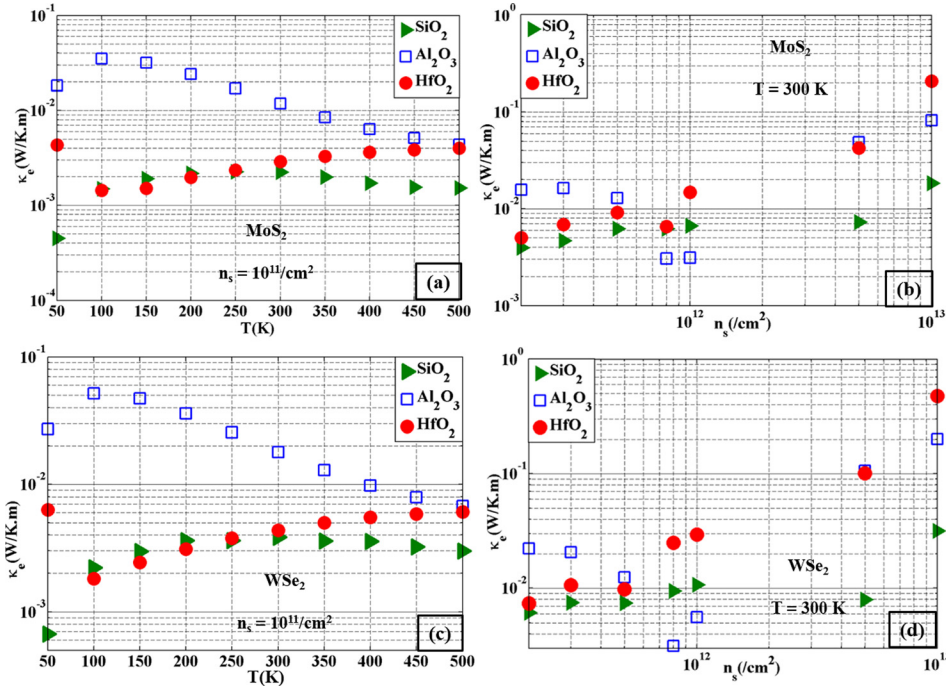
FIG. 7. (a) and (b) Dependence of thermal conductivity (electronic) for MoS_2 on temperature and electron density for different dielectric substrates; (c) and (d) similar plots for WSe_2. The plots with respect to n_s ((b) and (d)) begin from $n_s = 2 \times 10^{11}/cm^2$.

of substrate on Peltier coefficient is less compared to that on Seebeck coefficient since by definition, Peltier coefficient is a ratio of p_x and σ_x, both of which have similar effect from the substrates.

C. Thermal conductivity

Here, we calculate the electronic contribution to the thermal conductivity. As can be seen from the definition of thermal conductivity in terms of the transport coefficients in Section II, a high value of σ_x and K_x and a low value of p_x and B_x will produce a high electronic thermal conductivity (κ_e). p_x and B_x can both be shown to be the first order moment of the non-equilibrium part of the distribution function[32] (in our case, that is, g, the output from Rode's iteration) about the chemical potential. σ_x and K_x are the corresponding zero order and second order moments, respectively. So the magnitude of thermal conductivity strongly depends on the energy dependence of g which in turn is governed by the substrate. A strongly peaked g near the bottom of the conduction band (more scattering) reduces all the four coefficients, while a relatively flatter g (low scattering) increases all the coefficients and hence reduces κ_e. This is why κ_e will have a maxima for moderate inelastic scattering rates. This phenomenon can be clearly seen in Figs. 7(a) and 7(c) where Al_2O_3 produces the highest κ_e because of an intermediate inelastic scattering rate between SiO_2 and HfO_2. The cross-over of the curves for SiO_2 and HfO_2 reflects that the corresponding electronic distribution function follows an opposing trend (from a sharply peaked one to a flatter on for SiO_2 and the opposite way for HfO_2) as we increase the temperature.

Next, we take a look at the density dependence of κ_e shown in Figs. 7(b) and 7(d). The trend of κ_e with carrier density is a result of an interplay between mobility and carrier density. For SiO_2, it shows a decline in mobility with

increasing n_s (Figs. 4(c) and 4(d)) but the increasing n_s tries to increase the conductivity. Similarly, HfO_2 shows a mobility that is relatively independent of n_s and hence with increase in n_s, HfO_2 shows improving thermal conductivity. Al_2O_3 once again shows a clear non-monotonic behavior due to shifting of scattering mechanism from phonons to impurities. An important point to mention here is that the absolute values of κ_e reported in this work are for a TMD of thickness 5 Å and unlike, mobility and Seebeck coefficients, κ_e depend on thickness. However, the trends with temperature, density, and substrate are expected to be unaffected.

D. Thermo-electric figure-of-merit

The thermoelectric figure-of-merit[22] defined as $ZT = \frac{\alpha^2 \sigma T}{\kappa_e + \kappa_{ph}}$ is plotted in Figs. 8(a) and 8(b) at room temperature under varying electron density for different substrates. Here, σ is the electrical conductivity and κ_{ph} is the lattice contribution to thermal conductivity which we took to be recently reported value[24,44] of 19.5 W/K m. Comparing the magnitude of our calculated ZT with previously reported[22] values from ballistic transport calculation, we find that our ZT values are significantly low. The reason for this is the low σ obtained in our calculations due to the consideration of a highly diffusive transport. This argument can be verified if we take a look at the trend of ZT with electron density shown in Figs. 8(a) and 8(b). HfO_2 shows a significant improvement in ZT with increasing n_s which is a result of screening of phonon modes and absence of adequate impurity scattering due to strong dielectric environment screening. While SiO_2 and Al_2O_3 do not show such improvement since increasing n_s screens the phonon modes well but at the same time, enhanced impurity scattering (note $N_D = n_s$) does not let σ increase. To further verify that it is the diffusive transport that lowers ZT, we carry out the calculation with a very low
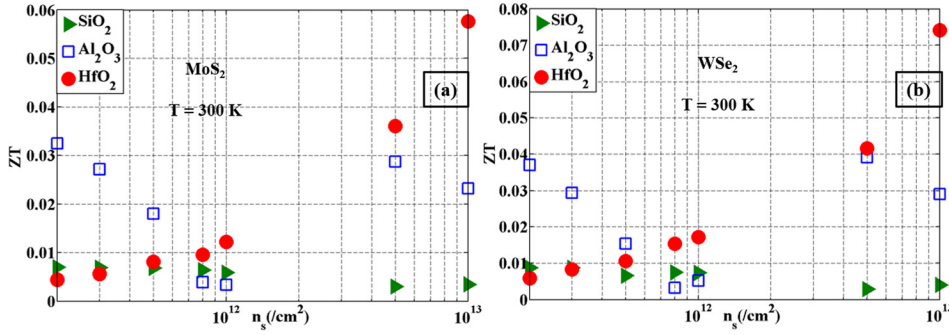
FIG. 8. (a) Dependence of ZT for MoS$_2$ on electron density; (b) similar plots for WSe$_2$. The plots with respect to n$_s$ ((b) and (d)) begin from n$_s$ = 2 × 10^{11}/cm^2.

impurity concentration but high electron density ($N_D = 10^{10}$ /cm^2, $n_s = 10^{13}$/cm^2) for both SiO$_2$ and HfO$_2$ at room temperature. While SiO$_2$ shows a 50 times improvement in ZT, HfO$_2$ shows negligible effect due to IPP dominated scattering. Higher electron density with low impurities could be achieved either by modulation doing or electrical doping by the application of a gate voltage. So the application of a gate voltage on SiO$_2$ to increase n_s with low trap density will improve ZT. In addition, high value of the considered phonon thermal conductivity (κ_{ph}) is another limitation on the calculated ZT values. Decreasing the phonon thermal conductivity through thermal engineering can also increase the ZT for MoS$_2$ and WSe$_2$.

VII. CONCLUSION

We have reported a theoretical calculation of thermoelectric transport coefficients of two TMDs: MoS$_2$ and WSe$_2$, taking into account a diffusive transport mechanism. The importance of taking into account a diffusive transport mechanism can be realized in the large influence of substrates on the transport coefficients. Effect of substrates is analyzed quantitatively, including plasmon-remote phonon coupling and dynamic screening. Even in the absence of additional impurities, the mobility of a TMD remains a bottleneck due to substrate induced remote phonon scattering in a high-dielectric environment.

An important issue to discuss is how the Seebeck coefficients (α) of the TMDs compare with conventional materials like GaAs. Reference 45 shows measured α for GaAs for an n-type doping of 7.7×10^{18}/cm^3 is around $100\,\mu$V/K at room temperature. The trade-off of α with temperature and doping density is similar to that observed in this work. A bulk SiGe alloy[17] also shows α around $100\,\mu$V/K at room temperature, a corresponding nano composite material Si$_{0.80}$Ge$_{0.20}$B$_{0.016}$ shows $\sim 160\,\mu$V/K, while In$_{0.09}$Ga$_{0.91}$N shows $\sim 300\,\mu$V/K for a doping density of 2×10^{18} /cm^3.[12] On the other hand, in this work, MoS$_2$ at room temperature showed a Seebeck coefficient of 500–$550\,\mu$V/K depending on the substrate chosen for a doping density of 10^{11}/cm^2 (a bulk analogue of this is roughly 2×10^{18}/cm^3 for a sample thickness of $5\,\text{Å}$). This increase in α is primarily due to an increased density of states at lower electron energies (near the Fermi Level) as pointed out for a quantum well structure.[16] Graphene[19] has been explored as a thermoelectric material but it suffers from a drawback of zero band gap since a minimum bandgap of $6\,k_BT$ is required[46] for optimum thermoelectric performance. TMDs are suitable from this perspective. The low thermal

conductivity (electronic) values are also promising for thermoelectric applications. In this work, the calculated ZT values are low because we include the mobility degradation in 2D materials due to remote interface phonons but we have not explored the effect of boundary scattering[16] of the phonon modes which causes κ_{ph} to degrade resulting in an improved ZT. Nevertheless, a possible improvement of ZT in a low-dielectric environment (e.g., SiO$_2$) can be made by either modulation doping or the application of a gate voltage to obtain high 2DEG density with low impurity concentration. Hence, to conclude, the TMDs produce a better Seebeck coefficient compared to other conventional materials, however selection of a proper substrate is crucial based on the temperature and carrier density to optimize performance.

APPENDIX A: SCATTERING STRENGTH OF THE IPP MODES

The decaying surface modes are given by Eq. (6). Applying Poisson's equation, we find out the corresponding polarization charge as

$$\rho_q^\nu(z) = \varepsilon_{sub}(q,\omega_q^\nu)A_{q,\omega_q^\nu}q^2 e^{qz} + \varepsilon_{TMD}(q,\omega_q^\nu)A_{q,\omega_q^\nu}q^2 e^{-qz}. \tag{A1}$$

Plugging this and Eq. (6) in Eq. (9), we get the mode amplitude

$$A_{q,\omega_q^\nu} = \sqrt{\frac{\hbar\omega_q^\nu}{q\left(\varepsilon_{sub}(q,\omega_q^\nu) + \varepsilon_{TMD}(q,\omega_q^\nu)\right)}}. \tag{A2}$$

But the dispersion relation in Eq. (7) gives $\varepsilon_{TMD}(q,\omega_q^\nu) + \varepsilon_{sub}(q,\omega_q^\nu) = 0$ which leads the mode amplitude to infinity. This problem arises since we have not separated out the contribution of the phonon modes in the dielectric constant of the substrate. There comes the necessity of defining the so-called "tailored" dielectric functions. The function $\varepsilon_{sub}^{\nu,-TOi}(q,\omega_q^\nu)$ in Eq. (10) is the dielectric function of the substrate with the substrate phonon mode TOi being frozen and is defined as[37] $\varepsilon_{sub}^{\nu,-TOi}(q,\omega_q^\nu) = \varepsilon_{sub}^\infty \frac{\omega_{LO,j}^2 - (\omega_q^\nu)^2}{\omega_{TO,j}^2 - (\omega_q^\nu)^2}$ ($i \neq j$) and the function $\varepsilon_{sub}^{\nu,+TOi}(q,\omega_q^\nu)$ gives the dielectric function of the substrate with the substrate phonon mode TOi being in "full" response and is defined as $\varepsilon_{sub}^{\nu,+TOi}(q,\omega_q^\nu) = \varepsilon_{sub}^\infty \frac{\omega_{LO,j}^2 - (\omega_q^\nu)^2}{\omega_{TO,j}^2 - (\omega_q^\nu)^2}\left(\frac{\omega_{LO,i}^2}{\omega_{TO,i}^2}\right)$. Hence, the contribution of the phonon mode TOi to the net mode amplitude is given as the difference between these two cases,[37]

$$A_{q,\omega_q^\nu} = \sqrt{\frac{\hbar\omega_q^\nu}{\varepsilon_0 q}\left(\frac{1}{\varepsilon_{sub}^{\nu,-TOi}(q,\omega_q^\nu) + \varepsilon_{TMD}(q,\omega_q^\nu)} - \frac{1}{\varepsilon_{sub}^{\nu,+TOi}(q,\omega_q^\nu) + \varepsilon_{TMD}(q,\omega_q^\nu)}\right)}. \tag{A3}$$

Multiplying the square of the mode amplitude with phonon content of each mode gives the square of the scattering strength which is Eq. (10) in the main text.

APPENDIX B: CONVERGENCE OF RODE'S ITERATIVE METHOD FOR 2D SCATTERING RATES

Equation (4) is the basic set up for Rode's iteration. The iteration continues until δ falls below a predefined tolerance where we define $\delta = \max(|g_{i+1} - g_i|)$. We set the tolerance value as 0.1% of $\max(g_0)$, g_0 is defined from RTA. In Fig. 9, we show different g_is' and the inset shows the rate of convergence which is exponential in nature.

APPENDIX C: ANALYTICAL EXPRESSION FOR SEEBECK COEFFICIENT OF NON-DEGENERATE 2D MATERIALS

From Eq. (1), the current density J_x can be written as

$$J_x = -\frac{e}{\Omega}\sum_{\boldsymbol{k}} \boldsymbol{v}g(k)\cos\theta. \tag{C1}$$

This is because the symmetric part of the electronic distribution function does not contribute to any current. From Eq. (4) in absence of the in-scattering term, $g(k)$ reduces to

$$g(k) = \frac{-\frac{eF}{h}\frac{\partial f_0(k)}{\partial k} - v\frac{\partial f_0}{\partial x}}{S_{out}(k) + 1/\tau_m(k)}. \tag{C2}$$

Short circuiting the ends of the devices gives $F = 0$, and hence

$$g(k) = \frac{-v\frac{\partial f_0}{\partial x}}{\Gamma(k)}, \tag{C3}$$

where $\Gamma(k) = S_{out}(k) + \frac{1}{\tau_m(k)}$ is the total out-scattering rate. Equation (C3) also follows from RTA. Plugging this expression of $g(k)$ in Eq. (C1) and carrying out the 2D angular integration in $\boldsymbol{k}-$ space, we get
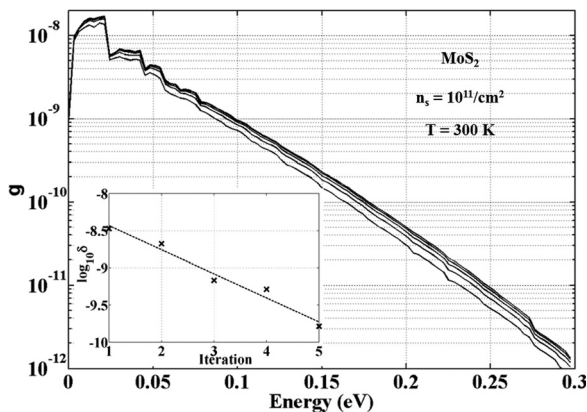

FIG. 9. Convergence of electronic distribution in Rode's iteration; (inset) rate of convergence with increasing iterations, only first few iterations are shown.

$$J_x = -\frac{4e\hbar}{\Omega E_N^{1-r}}\int E^{1-r}\frac{\partial f_0}{\partial x}dE. \tag{C4}$$

We took $\Gamma \propto E^r$ and E_N is just a normalization energy brought to preserve dimensions and does not affect the final results. We took care of spin and valley degeneracies though they are not important in current context. The job is to compute $\frac{\partial f_0}{\partial x}$. Using spatial charge homogeneity[26] ($\frac{\partial n}{\partial x} = 0$) and some algebraic manipulation, we obtain for a non-degenerate 2D material,

$$\frac{\partial E_F}{\partial x} = \frac{1}{T}\left(E_F - \frac{\int_0^\infty Ee^{-\eta}dE}{\int_0^\infty e^{-\eta}dE}\right)\frac{\partial T}{\partial x}, \tag{C5}$$

where $\eta = \frac{E-E_F}{k_BT}$, E_F is the chemical potential, and $\frac{\partial T}{\partial x}$ is the applied temperature gradient. Equation (C5), with a few more lines of algebra, reduces to $\frac{\partial E_F}{\partial x} = -k_B\frac{\partial T}{\partial x}$. Now for a non-degenerate semiconductor,

$$\frac{\partial f_0}{\partial x} = e^{-\eta}\frac{\partial \eta}{\partial x} \tag{C6}$$

and

$$\frac{\partial \eta}{\partial x} = -\frac{\eta}{T}\frac{\partial T}{\partial x} - \left(\frac{1}{k_BT}\right)\frac{\partial E_F}{\partial x}. \tag{C7}$$

Plugging $\frac{\partial E_F}{\partial x}$ from Eq. (C5) in Eq. (C7) and using that in Eq. (C6), we get

$$\frac{\partial f_0}{\partial x} = \frac{e^{-\eta}}{T}(1-\eta)\frac{\partial T}{\partial x}. \tag{C8}$$

Hence, the current density becomes

$$J_x = -\frac{4e\hbar}{\Omega E_N^{1-r}}\frac{\partial T}{T\partial x}\int E^{1-r}e^{-\eta}(1-\eta)dE. \tag{C9}$$

Now, we look at Eq. (5a) and see that σ_x is the coefficient of $\frac{\partial E_F}{\partial x}$. Hence, combining this view with Eqs. (C4), (C6), and (C7), we get

$$\sigma_x = -\frac{4e^2\hbar}{\Omega E_N^{1-r}}\frac{\partial T}{k_BT\partial x}\int E^{1-r}e^{-\eta}dE. \tag{C10}$$

Using Eq. (5a) and the definition of Seebeck coefficient, $\alpha = \frac{B_x}{\sigma_x T^2}$, where B_x is a transport coefficient in Eq. (5a), we can rewrite α as[26]

$$\alpha = -\frac{\left(\frac{J_x}{\sigma_x} - \frac{\partial\left(\frac{E_F}{e}\right)}{\partial x}\right)}{\frac{\partial T}{\partial x}}. \tag{C11}$$

We use the previously obtained relation $\frac{\partial E_F}{\partial x} = -k_B\frac{\partial T}{\partial x}$ and Eqs. (C9) and (C10) to calculate the right hand side of Eq. (C11). Usage of Gamma function leads to
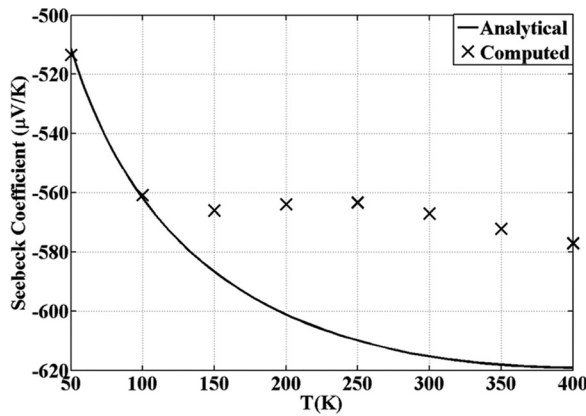
FIG. 10. Comparison of analytically calculated (from Eq. (C12)) Seebeck Coefficient with that calculated through detailed computation for MoS_2 on SiO_2 at $n_s = 10^{11}/cm^2$.

$$\alpha = -\frac{k_B}{e}\left(2 - r - \frac{E_F}{k_B T}\right). \qquad (C12)$$

Equation (C12) is the 2D analogue of the expression given in Ref. 26 for bulk materials. An expression for α in a quantum well structure was given in Ref. 18, but it does not explicitly show the dependence of α on the scattering parameter r as it most likely presumes $r = 0$. However, such assumption is not very accurate as our computation shows. A comparison of analytically calculated Seebeck coefficient for MoS_2 on SiO_2 at $n_s = 10^{11}/cm^2$ with that obtained with detailed numeric calculation is shown in Fig. 10. The deviation in higher temperature is obvious due to the futility of RTA in presence of inelastic scattering. However, the analytical expression is useful in gaining intuition on α in a 2D material.

[1] S. Kim, A. Konar, W. S. Hwang, J. H. Lee, J. Lee, J. Yang, C. Jung, H. Kim, J. B. Yoo, J. Y. Choi, Y. W. Jin, S. Y. Lee, D. Jena, W. Choi, and K. Kim, Nat. Commun. **3**, 1011 (2012).

[2] B. Radisavljevic, A. Radenovic, J. Brivio, V. Giacometti, and A. Kis, Nat. Nanotechnol. **6**(3), 147–150 (2011).

[3] M. Amani, M. L. Chin, A. G. Birdwell, T. P. O'Regan, S. Najmaei, Z. Liu, P. M. Ajayan, J. Lou, and M. Dubey, Appl. Phys. Lett. **102**(19), 193107 (2013).

[4] M. Buscema, M. Barkelid, V. Zwiller, H. S. van der Zant, G. A. Steele, and A. Castellanos-Gomez, Nano Lett. **13**(2), 358–363 (2013).

[5] S. Ghatak, A. N. Pal, and A. Ghosh, ACS Nano **5**, 7707–7712 (2011).

[6] Q. H. Wang, K. Kalantar-Zadeh, A. Kis, J. N. Coleman, and M. S. Strano, Nat. Nanotechnol. **7**(11), 699–712 (2012).

[7] W. C. W. Liu, J. Kang, and K. Banerjee, ECS Trans. **58**, 281–285 (2013).

[8] H. Zhou, C. Wang, J. C. Shaw, R. Cheng, Y. Chen, X. Huang, Y. Liu, N. O. Weiss, Z. Lin, Y. Huang, and X. Duan, Nano Lett. **15**(1), 709–713 (2015).

[9] A. Allain and A. Kis, ACS Nano **8**, 7180–7185 (2014).

[10] H. Sahin, S. Tongay, S. Horzum, W. Fan, J. Zhou, J. Li, J. Wu, and F. M. Peeters, Phys. Rev. B **87**(16), 165409 (2013).

[11] G. Zeng, J.-H. Bahk, J. E. Bowers, J. M. O. Zide, A. C. Gossard, Z. Bian, R. Singh, A. Shakouri, W. Kim, S. L. Singer, and A. Majumdar, Appl. Phys. Lett. **91**(26), 263510 (2007).

[12] A. Sztein, H. Ohta, J. E. Bowers, S. P. DenBaars, and S. Nakamura, J. Appl. Phys. **110**(12), 123709 (2011).

[13] J.-H. Bahk, Z. Bian, M. Zebarjadi, J. M. O. Zide, H. Lu, D. Xu, J. P. Feser, G. Zeng, A. Majumdar, A. C. Gossard, A. Shakouri, and J. E. Bowers, Phys. Rev. B **81**(23), 235209 (2010).

[14] B. Jalan and S. Stemmer, Appl. Phys. Lett. **97**(4), 042106 (2010).

[15] A. T. Ramu, L. E. Cassels, N. H. Hackman, H. Lu, J. M. O. Zide, and J. E. Bowers, J. Appl. Phys. **107**(8), 083707–083710 (2010).

[16] M. S. Dresselhaus, G. Dresselhaus, X. Sun, Z. Zhang, S. B. Cronin, T. Koga, J. Y. Ying, and G. Chen, Microscale Thermophys. Eng. **3**, 89–100 (1999).

[17] M. S. Dresselhaus, G. Chen, M. Y. Tang, R. G. Yang, H. Lee, D. Z. Wang, Z. F. Ren, J. P. Fleurial, and P. Gogna, Adv. Mater. **19**(8), 1043–1053 (2007).

[18] L. D. Hicks and M. S. Dresselhaus, Phys. Rev. B **47**(19), 12727–12731 (1993).

[19] P. Dollfus, V. Hung Nguyen, and J. Saint-Martin, J. Phys.: Condens. Matter **27**(13), 133204 (2015).

[20] Y. Yokomizo and J. Nakamura, Appl. Phys. Lett. **103**(11), 113901 (2013).

[21] H. Y. Lv, W. J. Lu, D. F. Shao, and Y. P. Sun, Phys. Rev. B **90**(8), 085433 (2014).

[22] W. Huang, H. Da, and G. Liang, J. Appl. Phys. **113**(10), 104304 (2013).

[23] W. Huang, X. Luo, C. K. Gan, S. Y. Quek, and G. Liang, Phys. Chem. Chem. Phys. **16**(22), 10866–10874 (2014).

[24] D. Wickramaratne, F. Zahid, and R. K. Lake, J. Chem. Phys. **140**(12), 124710 (2014).

[25] S. Kumar and U. Schwingenschlögl, Chem. Mater. **27**(4), 1278–1284 (2015).

[26] D. Rode, Semicond. Semimetals **10**, 1–89 (1975).

[27] Z.-Y. Ong and M. V. Fischetti, Phys. Rev. B **86**(16), 165422 (2012).

[28] Z.-Y. Ong and M. V. Fischetti, Phys. Rev. B **88**(16), 165316 (2013).

[29] N. Ma and D. Jena, Phys. Rev. X **4**(1), 011043 (2014).

[30] I. T. Lin and J.-M. Liu, Appl. Phys. Lett. **103**(8), 081606 (2013).

[31] K. Ghosh and U. Singisetti, J. Appl. Phys. **117**(6), 065703 (2015).

[32] M. Lundstrom, *Fundamentals of Carrier Transport* (Cambridge University Press, 2009).

[33] K. Kaasbjerg, K. S. Thygesen, and K. W. Jacobsen, Phys. Rev. B **85**(11), 115317 (2012).

[34] S. Q. Wang and G. D. Mahan, Phys. Rev. B **6**(12), 4517–4524 (1972).

[35] E. Evans and D. L. Mills, Phys. Rev. B **5**(10), 4126–4139 (1972).

[36] R. Chau, S. Datta, M. Doczy, B. Doyle, J. Kavalieros, and M. Metz, IEEE Electron Device Lett. **25**, 408–410 (2004).

[37] M. V. Fischetti, D. A. Neumayer, and E. A. Cartier, J. Appl. Phys. **90**(9), 4587 (2001).

[38] A. Konar, T. Fang, and D. Jena, Phys. Rev. B **82**(11), 115452 (2010).

[39] Z.-Y. Ong and M. V. Fischetti, Phys. Rev. B **88**(4), 045405 (2013).

[40] F. Stern, Phys. Rev. Lett. **18**(14), 546–548 (1967).

[41] B. K. Ridley, Rep. Prog. Phys. **54**, 169–256 (1991).

[42] P. F. Maldague, Surf. Sci. **73**, 296–302 (1978).

[43] B. A. Glavin, V. I. Pipa, V. V. Mitin, and M. A. Stroscio, Phys. Rev. B **65**(20), 205315 (2002).

[44] V. Varshney, S. S. Patnaik, C. Muratore, A. K. Roy, A. A. Voevodin, and B. L. Farmer, Comput. Mater. Sci. **48**(1), 101–108 (2010).

[45] A. Amith, I. Kudman, and E. F. Steigmeier, Phys. Rev. **138**(4A), A1270–A1276 (1965).

[46] J. O. Sofo and G. D. Mahan, Phys. Rev. B **49**(7), 4565–4570 (1994).

[47] Z. Jin, X. Li, J. T. Mullen, and K. W. Kim, Phys. Rev. B **90**(4), 045422 (2014).

[48] R. Singh, R. Scholz, S. H. Christiansen, and U. Gösele, Semicond. Sci. Technol. **23**(4), 045007 (2008).

[49] A. Kumar and P. K. Ahluwalia, Phys. B: Condens. Matter **407**(24), 4627–4634 (2012).